Universities of Leeds, Sheffield and York
http://eprints.whiterose.ac.uk/

On the coherence/incoherence of electron transport in semiconductor heterostructure optoelectronic devices

P. Harrison, D. Indjin, I. Savić, Z. Ikonić, C. A. Evans, N. Vukmirović, R. W. Kelsall, J. McTavish, V. D. Jovanović and V. Milanović[*]

School of Electronic and Electrical Engineering, University of Leeds, Leeds LS2 9JT, U.K.;
[*]School of Electrical Engineering, 11120 Belgrade, Serbia

ABSTRACT

This paper compares and contrasts different theoretical approaches based on incoherent electron scattering transport with experimental measurements of optoelectronic devices formed from semiconductor heterostructures. The Monte Carlo method which makes no *a priori* assumptions about the carrier distribution in momentum or phase space is compared with less computationally demanding energy-balance rate equation models which assume thermalised carrier distributions. It is shown that the two approaches produce qualitatively similar results for hole transport in p-type $Si_{1-x}Ge_x/Si$ superlattices designed for terahertz emission. The good agreement of the predictions of rate equation calculations with experimental measurements of mid- and far-infrared quantum cascade lasers, quantum well infrared photodetectors and quantum dot infrared photodetectors substantiate the assumption of incoherent scattering dominating the transport in these quantum well based devices. However, the paper goes on to consider the possibility of coherent transport through the density matrix method and suggests an experiment that could allow coherent and incoherent transport to be distinguished from each other.

Keywords: Quantum cascade laser, quantum well infrared photodetector, electron transport, electron scattering, density matrix

1. INTRODUCTION

Quantum cascade lasers (QCLs) have demonstrated an impressive extension of the infrared frequency range. Since the first terahertz QCL laser action [1], recent reports have given wavelengths as along as 250μm (1.2 THz) [2] and at 355μm (830 GHz) with the support of external magnetic field [3]. At the same time several mid-infrared GaAs/AlGaAs QCLs devices have achieved pulsed room temperature operation, for example the triple quantum well QCL [4] emitting at 9.3μm, the bound to continuum QCL [5] at 11μm and the superlattice QCL [6] at 12.6μm. In addition continuous wave operation up to 150K has also been reported [7]. The numerous quantum wells separated by often thin barriers and the single carrier type (these are unipolar devices) make QCLs an ideal testbed for studies of quantum mechanical transport and this is the focus of this paper.

2. THEORETICAL APPROACHES

Let $H = H_0 + H'$ be the Hamiltonian of the structure under consideration, where $H_0 = \sum_\alpha \varepsilon_\alpha a_\alpha^+ a_\alpha$ is the interaction-free part of the Hamiltonian with single-particle eigenenergies ε_α with a_α^+ and a_α being the creation and anihillation operators of the carrier in single-particle state α. The interaction of carriers with phonons, impurities, carrier-carrier interaction and other interaction terms are contained in H'. A fully quantum mechanical microscopical description of the carrier dynamics in nanostructures could start from the single-particle density matrix $\rho_{\alpha\beta} = \langle a_\alpha^+ a_\beta \rangle$ whose diagonal elements represent the occupancies of single particle states and off-diagonal elements describe the coherent processes. From the equation of motion of the operators a_α in the Heisenberg picture

$$i\hbar \frac{\mathrm{d}a_\alpha}{\mathrm{d}t} = [H_0 + H', a_\alpha] \tag{1}$$

one gets that the elements of the density matrix satisfy the following time-dependent equations:

$$i\hbar\frac{\mathrm{d}}{\mathrm{d}t}\langle a_\alpha^+ a_\beta\rangle = (\varepsilon_\alpha - \varepsilon_\beta)\langle a_\alpha^+ a_\beta\rangle + \langle[H', a_\alpha^+ a_\beta]\rangle \tag{2}$$

The first term on the right hand side in the previous equation describes the coherent oscillations between states α and β, while the second term describes the interaction. It is currently thought [8] that coherent processes play only a minor role in the transport in quantum cascade structures where the existence of many different layers, interfaces, alloys, other charge carriers, ionised impurities and many active phonon modes from the finite temperature lead to high levels of carrier scattering [9–11]. This gives very short decoherence times in the range of 50 fs–1 ps implying that the transport is dominated by *incoherent* scattering. Different opinions however do exist and it has been argued that coherent transport is not insignificant for the particular case of transport through a wide barrier in a terahertz quantum cascade laser where the small anti-crossing energies allow for a component of resonant tunnelling [12].

Given this dominance of incoherent scattering it is therefore a usual approximation to neglect the off-diagonal terms in the density matrix thus significantly reducing the number of variables one has to handle with. In the Markov approximation [13] the density matrix equations then reduce to semiclassical Boltzmann equations:

$$\frac{\mathrm{d}f_\alpha}{\mathrm{d}t} = \sum_\beta [f_\beta(1-f_\alpha)W_{\beta\alpha}) - f_\alpha(1-f_\beta)W_{\alpha\beta})] + \sum_{\beta\gamma\delta}[f_\gamma f_\delta(1-f_\alpha)(1-f_\beta)W_{\gamma\delta\alpha\beta} - f_\alpha f_\beta(1-f_\gamma)(1-f_\delta)W_{\alpha\beta\gamma\delta}] \tag{3}$$

where f_α are the diagonal elements of the density matrix operator, $W_{\alpha\beta}$ are the single-particle scattering rates from state α to state β and $W_{\alpha\beta\gamma\delta}$ are two-particle scattering rates.

There are several ways to solve the Boltzmann transport equation. The Monte Carlo method [14] is a stochastic approach which *simulates* the trajectories of a representative ensemble of electrons or holes. In the limit of a large number of charge carriers and inclusion of all possible scattering rates the Monte Carlo method is capable of producing a solution of arbitrary accuracy. A simplifying assumption that the charge carriers in any particular band or subband can be approximated by Fermi-Dirac statistics [10] allows the Boltzmann transport equation to be replaced by simpler and hence less computationally demanding rate equations. In the case of a system with discrete energy levels, such as quantum dots or quantum wells in a magnetic field, the Boltzmann equations are already in the form of rate equations for the occupancies of energy levels, and by solving them one obtains the same level of accuracy as with Monte Carlo simulations in quantum wells, see for example [15, 16].

It will be demonstrated in this work that this philosophical approach of incoherent transport, which can be solved by Monte Carlo or rate equation methods, has a wide application across many electronic and opto-electronics devices, including near- and mid-infrared as well as terahertz quantum cascade lasers, superlattices, quantum well infrared photodetectors and quantum dot infrared photodetectors.

3. MONTE CARLO VS. RATE EQUATIONS: THE CASE OF P-DOPED $\mathrm{SI}_{1-X}\mathrm{GE}_X/\mathrm{SI}$ QUANTUM CASCADE STRUCTURES

Vertical (i.e. perpendicular to the layers) hole transport in a semiconductor heterostructure offers perhaps the most demanding challenge for physical modelling because of the multiple and anisotropic energy bands. Nonetheless there has been a large research effort in this area, related to the efforts to develop infrared sources using the quantum cascade approach [17] based on Si/SiGe heterostructure, which would therefore be integratable with standard CMOS electronics. The use of p-type material offers the further advantage of the possibility of vertical cavity surface emitting lasers (VCSELs) [18].

The hole band structure in p-$\mathrm{Si}_{1-x}\mathrm{Ge}_x/\mathrm{Si}$ was calculated using the $6{\times}6$ $\mathbf{k}\cdot\mathbf{p}$ method whose accuracy is very good for structures with subband spacings in the range of tens of meV [19]. The method accounts for the mixing of heavy-hole, light-hole and spin-orbit split-off valence band states, and therefore accounts for the nonparabolicity and warping of the quantum well subbands. For the purpose of hole scattering calculation the band structure (energies and wave functions) are tabulated on a 2D grid of in-plane wave vector ($\mathbf{k}_\parallel$) points, which cover an irreducible wedge of the in-plane Brillouin zone (1/8 of the full zone for [001] growth), of sufficient extent that
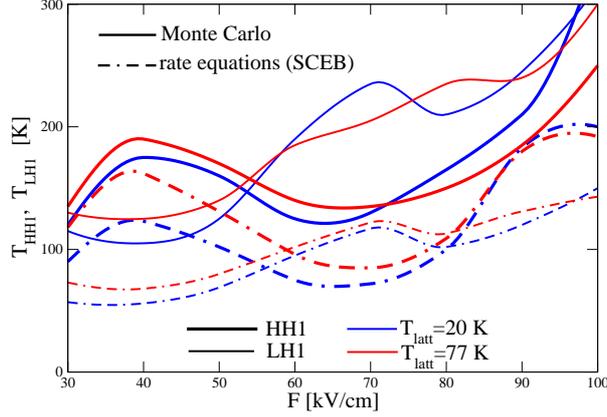
Figure 1. The HH1 and LH1 subband temperatures versus bias dependence calculated for the $Si_{1-x}Ge_x/Si$ quantum cascade structure described in the text, for different lattice temperatures T_{latt}, using either the MC or the SCEB rate equation method. Hole–hole scattering is not included.

esentially all states accessible for holes are included. The states outside this wedge can then be constructed using the symmetry properties, by rotation. The second ingredient in analysing transport is to assign all the states in a cascade to its individual periods, i.e. to find all states assigned to a particular 'reference' period, from which one can then construct all other states in a cascade by space translation and shift of energy. This is essential in setting up a tight-binding-like description of scattering transport. The peculiarity of hole states is that this procedure has to be done independently for each $\mathbf{k}_\parallel$ grid point, in contrast to the case of electron states in n-doped cascades, where the assignment procedure has to be done just once because the wavefunctions do not depend on $\mathbf{k}_\parallel$.

We next calculate the microscopic ($\mathbf{k}_\parallel$-dependent) scattering rates between all pairs of states on the grid. The important scattering mechanisms for holes in $Si_{1-x}Ge_x/Si$ which were included in the transport calculations, are the deformation potential scattering (acoustic and optical phonons, in the later case the Ge-Ge, Ge-Si and Si-Si modes), alloy disorder scattering, and carrier-carrier scattering. There is no polar LO phonon scattering in (non-polar) $Si_{1-x}Ge_x$ material, i.e. optical phonons interact with holes only via the deformation potential, and hence the major scattering mechanism in III/V's is absent in this material. These microscopic scattering rates can be further used in two ways:

(i) One is to set up the system of population balance equations for each cell on the $\mathbf{k}_\parallel$-grid for all the subbands included in consideration, and find the steady-state population distribution, or track the time evolution of the population. This is the Boltzman equation approach, and the method usually employed to solve it is the Monte Carlo (MC) method. The output then contains detailed information on the occupancy of each cell, i.e. the hole distribution over $\mathbf{k}_\parallel$ points of each subband. The population of subbands can then be found by integrating over all the cells [20].

(ii) The other way is to assume that the carrier distribution over the in-plane wave vector states (cells) within a subband is quasi-equilibrium like, having the form of a Fermi-Dirac (FD) distribution function, which enables the evaluation of averaged scattering rates, weighted by such a distribution. This results in a system of rate equations (RE) for the subband populations. Their number is hugely reduced from the number of equations present in the discretised form of the Boltzmann equation, and the system can be solved much faster. When imposing the FD form of the carrier distribution over $\mathbf{k}_\parallel$-states of each subband, however, one can decide to assign to it a fixed temperature (e.g. equal to the lattice temperature, or to some other reasonably chosen value), or to leave the subband temperature as yet another unknown to be determined (in addition, different subbands can be allowed to have different temperatures, or can be further assumed to have the same temperature, but generally different from that of the lattice). In the first case, one has the simple 'particle-only' rate equations and in the later the 'self-consistent' energy-balance (SCEB) rate equations, where not just the subband populations but also their energy content is tracked [21].
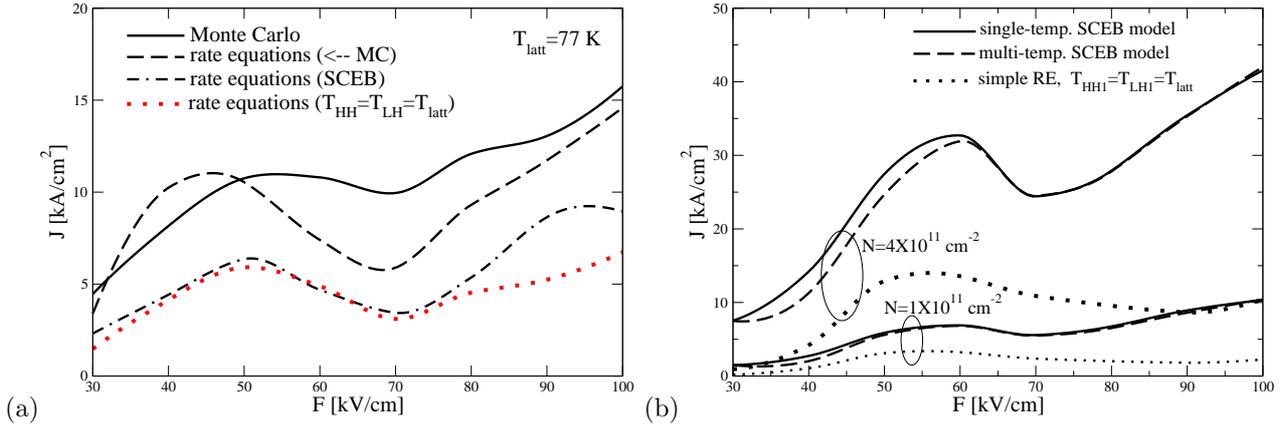
Figure 2. The current density versus bias dependence for the structure described in the text, calculated (a) by the MC, the SCEB rate equations, and by the simple, 'particle-only' rate equation method with the carrier temperature set equal to T_{latt} and to the values delivered by the MC simulation ($\leftarrow$MC) and (b) by the SCEB rate equation method with independent or equal subband temperatures, and by the simple rate equation method. Hole–hole scattering is included.

In order to find the degree of accuracy involved in each of these approximations we have performed numerous calculations. Consider the simplest nontrivial quantum cascade structure, that has two relevant states per period (their energies being such that both can be expected to have a sizeable population under the chosen range of operating biases, while any higher states are almost empty). The structure has one 4.41 nm wide $Si_{0.7}Ge_{0.3}$ quantum well and one 2.15 nm wide Si barrier in a period, and can be grown strain-balanced on a $Si_{0.8}Ge_{0.2}$ virtual substrate. Its first excited state (LH1) is 28 meV above the lowest (HH1), and the alignment at $\mathbf{k}_{\parallel} = 0$ of HH1 from the preceeding period with LH1 from the next period occurs at 42 kV/cm. For $\mathbf{k}_{\parallel} \neq 0$ the alignment occurs at somewhat different biases, due to subband warping and nonparabolicity. The structure can be considered as a simple prototype quantum cascade laser (QCL) [20], with emission occuring on the diagonal (cross-period) transition HH1$\rightarrow$LH1 for biases exceeding the alignment bias, provided it remains free from domain formation [22].

To aid a comparison between the MC and 'particle-only' or SCEB rate equation methods we have switched off the hole–hole scattering. The in-plane hole distributions delivered by the MC simulations generally resemble the FD distribution, but are quantitatively different to an extent which depends on the bias [21]. In Fig. 1 we plot the bias dependence of the subband temperatures calculated by the SCEB or extracted from the MC simulation. It is important to note that the MC method itself does not have any intrinsic carrier temperatures, so these are calculated from the in-plane distributions, requiring that the actual average of hole kinetic energy equals the value which would be obtained by giving an *effective* MC temperature to the FD distribution. Somewhat different values might be obtained by defining them in some other reasonable manner (e.g. by requiring the best congruence of MC and FD distributions, etc.). There is therefore a degree of ambiguity in the carrier temperatures extracted from MC method. However, the general feature present in Fig. 1, and consistent with transport simulations for electrons [23], is that although the curves are qualitatively similar, the carrier temperatures deduced from the MC method are higher than those calculated from the SCEB rate equation approach.

The calculated hole current density (Fig. 2(a)) reflects this discrepancy. A part of it is specific to holes: the $\mathbf{k}_{\parallel}$-dependent band mixing, coupled with different penetration of heavy- and light-hole components through the barrier, causes a sensitivity of current to the precise form of the in-plane distribution of holes, as highlighted by comparing the MC results against those obtained by directly inserting the MC temperatures into 'particle-only' rate equations (which clearly is of academic interest, rather than a technically useful approach, but gives insight into effects stemming purely from the non-FD form of the distribution). This effect is largely absent for electrons with their simpler subband structure. It should be noted, however, that the discrepancy between the MC and SCEB simulations shown here is artificially enhanced by the absence of (intra-subband) hole–hole scattering, which is a much more efficient mechanism which drives the distribution towards an FD-like form than is the

acoustic phonon scattering which is included in these simulations. Therefore, in real situations the non-FD character of the carrier distribution itself has a relatively small impact on the macroscopic transport properties (and, in the case of electrons, no impact on their optical activity). On the other hand, comparing the results found by the different types of rate equation method clearly shows the importance of carrier heating effects, which must be taken into account, particularly for lower values of lattice temperature. As for the subband populations, which in fact is the most important parameter for QCL operation, the discrepancy between different methods turns out to be much smaller, and this feature enables one to employ rate equations (with the energy balance accounted for, not the simple, 'particle-only' rate equations) for efficient simulation of QCL operation, despite the approximate nature of the method.

Finally, it is of considerable practical interest to explore the importance of allowing independent subband temperatures, in contrast to assuming all of them to be equal (but still different from the lattice temperature), because solving the system of rate equations is much faster in the latter case. In Fig. 2(b) we give a comparison of the SCEB rate equation results, found with either of the two choices, this time with hole–hole scattering taken into account. The self-consistently calculated but imposed-common temperature of the holes is found approximately equal to the weighted average of the individual subband temperatures. The agreement for the curent density, as well as for the subband populations (not shown) is quite good, indicating that the common-temperature model is yet another reasonable approximation. This should be an even better approximation for electrons than for holes, as in the latter case the more complicated band structure may still give rise to somewhat different optical responses.

4. RATE EQUATIONS VERSUS EXPERIMENT IN N-TYPE III-V TERAHERTZ QUANTUM CASCADE LASERS
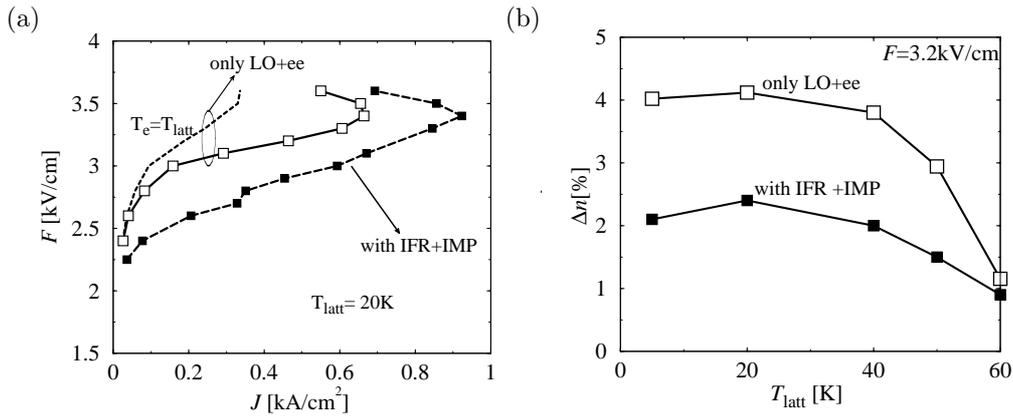

Figure 3. (a) Electric field versus current density characteristics for the first GaAs/Ga$_{1-x}$Al$_x$As THz QCL [1] calculated at a lattice temperature T_{latt}=20 K, (b) The population inversion Δn as a function of the lattice temperature in the first GaAs/AlGaAs THz QCL [1].

Following well documented applications of the rate equations method to quantum cascade lasers, see for example [24–26], Figure 3(a) shows the calculated electric field–current density characteristics at a lattice temperature of 20K for the first terahertz QCL which was realized by Köhler *et al.* [1]. An initial self-consistent calculation was performed under the approximation that electron temperatures are equal to the lattice temperature, following this, kinetic energy rate equations were included which allowed calculation of the electron temperature under the assumption of equal electron temperatures in all subbands [10, 27]. All relevant electron–LO phonon and electron–electron scattering mechanisms were included in the calculations. Under the assumption that the electron temperature remains equal to the lattice temperature, i.e. $T_{\text{e}} = T_{\text{latt}}$ (as depicted by the dotted line in Fig. 3(a)), the F–J curves show current density saturation and negative differential resistance (NDR) features at very low currents, which are not consistent with the experimental results [28]. We find with the full calculation
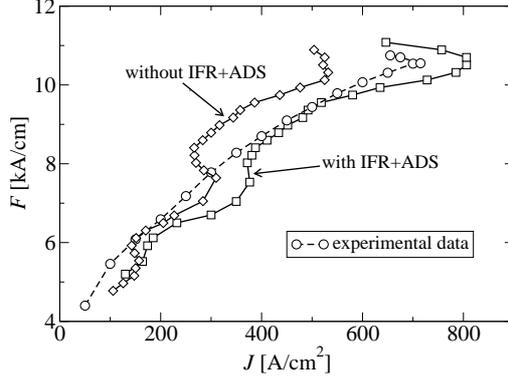
Figure 4. Electric field versus current density characteristics in a THz QCL based on the LO-phonon depopulation mechanism [32] calculated at a lattice temperature T_{latt}=77 K when electron-LO phonon, electron-electron (EE) and electron-ionised impurity (IMP) scattering is included (diamonds) and when interface roughness (IFR) and alloy disorder (ADS) scattering is included (squares). The dashed line with circles represents the experimental data.

(solid line with open squares), which includes kinetic energy balance, i.e. a self-consistent energy balance (SCEB) approach, that current saturation is predicted at $\sim$ 680 A/cm^2 which is in reasonable agreement with that measured at $\sim$ 820 A/cm^2. The discrepancy is probably related to the fact that to limit the computational demands of the problem we have limited the calculations to include only the electron-LO phonon and electron–electron scattering.

Although the simulation is already computationally demanding, particularly in a superlattice-like structures with a number of quantum wells and barriers (i.e. a large number of subbands in any one of the QCL periods), we have extended the present model to include electron–ionised impurity (IMP) and interface roughness (IFR) scattering. Whilst this makes the model more realistic, the disadvantage is that for the first time in the model a parameter has been introduced, namely the extent of the interface roughness. To keep things as justifiable as possible the extent of the interface roughness has not been used as a variable parameter to obtain the best fit with experiment, it has been taken directly from experimental measurements in similar heterostructures. In particular, the mean height of the roughness was taken to be one monolayer (2.83 Å) with a correlation length of 50 Å [29, 30]. The calculations above were repeated with these additional scattering mechanisms and the calculated electric field–current density characteristics, again at a lattice temperature of 20 K are also shown in Fig. 3(a) (dashed line with full squares). The calculated saturation current is now $\sim$ 910 A/cm^2 which is considerably closer but slightly higher than the measured value of $\sim$ 820 A/cm^2. In this case, the discrepancy is probably due to an overestimation of the interface roughness correlation length.

The calculations also show that, up to the NDR feature, the average electron temperature T_{e} can be approximated as a linear function $T_{\text{e}} \approx T_{\text{latt}} + \alpha_{\text{e–l}}J$, where $\alpha_{\text{e–l}} \sim 52$ K/(kAcm^{-2}). The most recent micro-probe photoluminscence measurements in a similar terahertz QCL [31], suggests $\alpha_{\text{e–l}} \sim 69 - 77$ K/(kAcm^{-2}). The elevated electron temperature is due to the inefficiency of low energy inelastic scattering at cooling the electron distributions which heat until they can begin to emit intrasubband LO phonons.

The population inversion Δn as a function of the lattice temperature is shown in Fig. 3(b). When including only electron–LO phonon and electron–electron scattering, the calculated population inversion of Δn=4.2% at T_{latt}=10 K is in very good agreement with the results of a Monte Carlo simulation [33], which was also limited to the same scattering mechanisms. At lower lattice temperatures (below 30 K) electron–electron and electron-LO phonon scattering vary slowly with temperature, which makes the active region laser level lifetimes almost insensitive to temperature. However, above 30 K another effect appears: the electron distributions broaden which overcomes the small energy spacing between the upper and lower laser levels and LO phonon emission becomes possible. As a result of this thermally activated LO-phonon emission from the upper laser state, the population inversion decreases above $\sim$ 50 K, hence an increase in the threshold currents is expected. Although less prominent, such an effect is also found when interface roughness and ionised impurity scattering mechanisms

are included, see also Fig. 3(b). In the latter case, temperature independent interface roughness scattering is comparable to electron-phonon scattering at very low temperatures and, due to the somewhat higher temperature of the upper laser level, thermally activated LO phonon scattering is more efficient, all of which results in a further decrease of inversion below $\Delta n = \sim 2.5$ % The maximum operating temperature of the particular device design is estimated to be 75–80 K, again in good agreement with experimental findings in the first THz QCL [1].

Another set of calculations was performed for a different type of THz QCL design which is based on the resonant LO phonon depopulation mechanism [32]. This structure exhibits a maximum operating temperature of 130 K in pulsed mode and 78 K in continuous wave *cw* mode. The rate equation model was extended to include another 'close range' scattering mechanism, that of alloy disorder (ADS) scattering. The calculated current–voltage characteristic at 77 K is shown in Fig.4. Without IFR and ADS scattering the maximum current density was calculated as ~ 520 A/cm^2 which is a little lower than the measured value of ~ 750 A/cm^2. Again, including additional scattering mechanisms, this time IF and ADS, the calculated electric field–current density F–J I-V characteristic is in much better agreement with measurement, as clearly indicated in Fig. 4. Furthermore, our SCEB rate equation method gives a population inversion of $\sim$5% at 77 K which is consistent with a recent Monte Carlo simulation in a similar structure at low lattice temperatures, see for example [34–36].

5. RATE EQUATIONS VERSUS EXPERIMENT IN MID-INFRARED QUANTUM CASCADE LASERS

The doping level in the active region of a QCL is an important parameter with a particular influence on the dynamic working range of the device. Due to the superior device performance of mid-infrared devices with 45% Al-content there has been a demand for a comprehensive experimental and theoretical analysis of these designs. With this aim injector sheet doping densities have been analysed in the range 2–14×10^{11}cm^{-2}. We have extended the SCEB approach to include the effects of the free carrier distribution (the Hartree potential) on the effective band profile as well as to include ionised impurity scattering which is relevant for the higher doping conditions [37]. As the non-equilibrium carrier distribution is not pre-defined, the Schrödinger and Poisson equations as well as the system of scattering rate equations are intrinsically coupled. As a consequence, only convergence of both processes (self-self-consistency) will give an accurate solution for the carrier distribution. In this particular case, the following relevant scattering mechanisms have been taken into account: electron-phonon, electron-electron and ionised impurity scattering. The latter is expected to be an important scattering interaction at the higher doping levels. An initial set of calculations showed that the scattering owing to acoustic phonons can be assumed to be negligible in the analysis of mid-infrared QCLs because of their large level energy separation and relatively high operating temperature.

The electron transport in the $\lambda \sim 9\mu m$ GaAs/Al$_{0.45}$Ga$_{0.55}$As QCL reported in Ref. [4] was simulated, and the non-equilibrium distribution over subbands for injector doping (sheet electron) densities ranging from 2×10^{11} to 14×10^{11}cm^{-2} calculated at 77 K. For the conventional doping levels of 4–6×10^{11}cm^{-2} the self-consistent band-bending owing to the specific electron distribution is not prominent and does not considerably change the electronic structure (energies and wavefunctions) as shown in Fig. 5a. The calculated current density-electric field characteristic is well supported by the original experimental data [4,38]. However, for higher doping densities the band profile becomes quite different, see Fig. 5b. This is especially important in the working regime close to resonant alignment. i.e. just below the current density saturation and before the fall of the optical power. For lower doping, and an applied field of 60kV/cm, the coupling between the lowest injector state and upper laser level is quite strong and the system is close to resonance. Quite the opposite occurs at higher doping and for the same value of applied field the levels are now widely separated and the system is far from reaching the resonant condition. This is a direct consequence of the electron-ionised donor separation within each QCL period, forming v-shaped local field domains. This domain formation is especially pronounced at high doping levels.

We also explored the behaviour of the maximal current density (the current density just before the current saturation) as well as the maximal gain in the simulated QCL. In Fig. 6(a) the saturation current density (which corresponds to the resonant alignment of the lowest injector state and the upper laser level) and the maximal gain corresponding to this current are presented as a function of the doping density. The saturation current exhibits a linear dependence for doping densities up to 8×10^{11}cm^{-2} and clear saturation for higher doping levels. The explanation for such behaviour is domain formation, as mentioned earlier. As the doping
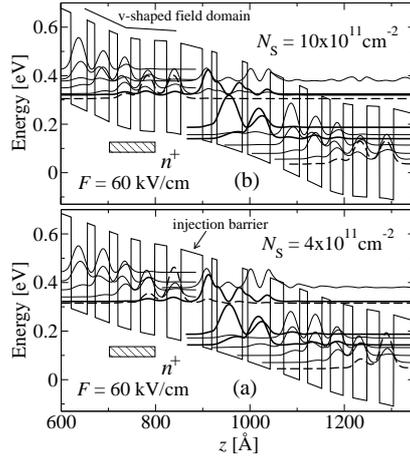
Figure 5. A schematic diagram of the calculated self-self-consistent conduction band profile, quasi-bound energy levels and wavefunctions squared of a GaAs/Al$_{0.45}$Ga$_{0.55}$As QCL for sheet carrier densities of (a) 4×10^{11} and (b) 10×10^{11}cm^{-2} and an applied external electric field of 60kV/cm. The laser levels are shown in bold and the lowest injector state by dashed lines. The doped region of the injector is also indicated.

level increased, the influence of the Hartree potential on the band profile becomes more important, preventing resonant alignment in the working range of applied electric fields. The v-shape local domain tilts the doped part of the injector region, thus increasing the local electric field, and lowering the lowest injector state energy. In contrast, the local electric field in the lower part of the injector region (close to the injection barrier) is decreased in order to preserve a constant bias across the period, and the region is tilted in the opposite direction increasing the upper laser level energy. Both effects act to separate the lowest injector and the upper laser level and consequently prevent resonant tunnelling. The inset of Fig. 6(a) shows the experimental measurements of the saturation currents for different doping densities. Results for both the 45% and 33% aluminium mole fraction in QCLs barriers are taken into account as the difference in structures has a minimal affect for 77 K temperature operation [4]. The calculated values of the saturation currents are somewhat higher than measured, however, the experimental behaviour is clearly comparable to theoretical results. The saturation current exhibits similar behaviour showing a clear saturation at the higher doping densities as theoretically predicted. Following this work, effect of saturation of maximal current for higher levels of injector doping has been measured in another GaAs-base mid-infrared laser structure [38]. More recently the effect has been observed experimentally in InAs/AlGaSb [39] and InGaAs/InAlAs/AlAs [40] mid-infared QCLs. The influence of the saturation of the maximal current can also be seen in the maximal gain.

The electron temperature in the single temperature approximation, calculated as a function of current density at 80K and 240K, for different doping densities is presented in Fig. 6(b) [41]. Although the dependences are well fitted by a quadratic function (dashed lines), for the range of working current densities, the quadratic bowing is rather small, thus a linear functional form can be adopted and commonly characterised by a electron temperature-current coupling constant. For a fixed value of the current density, a decrease of the electron temperature with doping has been observed. A more macroscopic explanation can be presented in terms of an effective decrease of input electrical power P_{E}, i.e. the same value of the current density at higher doping corresponds to the lower applied bias than in case of a lower doping. Also, the power per electron decreases as the number of electrons increases. Hence, for the same current density, the electrons in the QCL, in the higher doping regime, need to heat up less than for lower doping, in order to facilitate a LO-phonon emission and an efficient heat dissipation. This was confirmed by calculating the ratio between the relative increase in electron temperature and power of each individual electron $(T_{\mathrm{e}} - T_{\mathrm{L}})/(P_{\mathrm{E}}/N_s)$ which shows almost constant behaviour for all doping levels. Consequently, the coupling constant drops with increased doping from 10.3K/kAcm^{-2} at 4.1×10^{11}cm^{-2} to 7.1K/kAcm^{-2} at 6.5×10^{11}cm^{-2} at 80K and from 22.2K/kAcm^{-2} at 4.1×10^{11}cm^{-2} to 14.2K/kAcm^{-2} at 6.5×10^{11}cm^{-2} at 240K. The value at 4.1×10^{11}cm^{-2} at 240K is in good agreement with published experimental
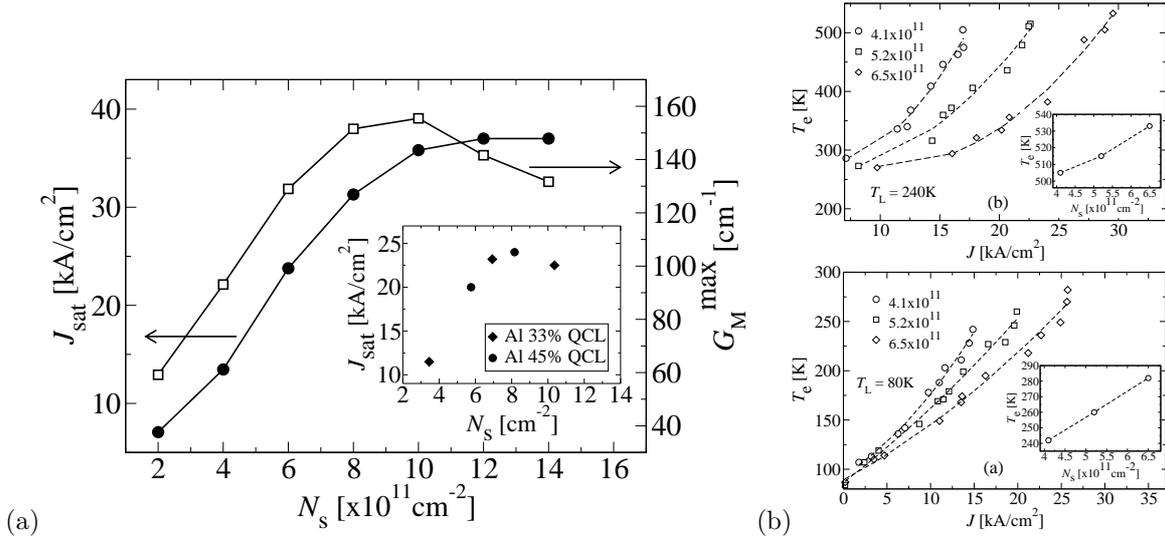
Figure 6. (a) Simulated saturation current density (circles) and maximal modal gain (squares) as functions of the doping density. Inset: Experimental measurements of the saturation current for 45% Al (circles) and 33% Al (diamonds) QCL devices for different doping densities, (b) Calculated electron temperature as a function of the current density for the three doping densities of $4.1 \times 10^{11} cm^{-2}$ (circles), $5.2 \times 10^{11} cm^{-2}$ (squares) and $6.5 \times 10^{11} cm^{-2}$ (diamonds) at the lattice temperatures of (a) 80 K and (b) 240 K. Quadratic fits are given by dashed lines. Insets: The maximal simulated electron temperature as a function of the injector doping density.

value of $\sim 28K/kAcm^{-2}$ determined from micro-probe photoluminescence measurements [42] . The maximal value of the electron temperature, which corresponds to the current density just before saturation, is found to increase linearly with doping. The evaluated increase was around 40 K (i.e. 17%) at 80 K in comparison with $\sim 20K$ (6%) at 240 K. The latter is due to reduced LO-phonon scattering sensitivity to doping density change at high temperatures.

6. RATE EQUATIONS VERSUS EXPERIMENT IN QUANTUM WELL INFRARED PHOTODETECTORS (QWIPS)
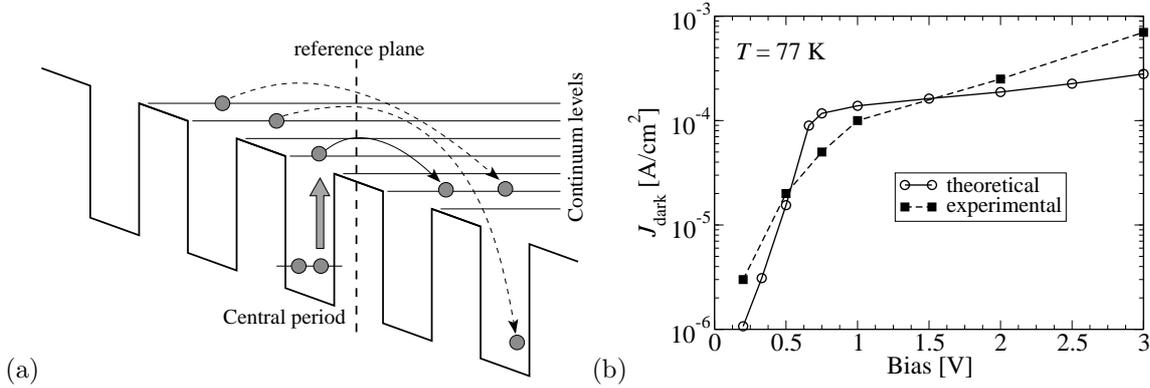

Figure 7. (a) Schematic diagram of the conduction band profile and the principles behind the QWIP physical model, (b) The calculated (solid line and circles) and the experimental (dashed line and squares) dark current density versus bias potential for a 8.5 μm QWIP at 77 K.

Quantum well infrared photodetectors (QWIPs) are similar to quantum cascade lasers in that they are unipolar devices and are usually made from biased periodic III-V semiconductor heterostructures. For a review

of recent developments in QWIPs see, for example [43]. In the first instance they appear simpler than QCLs in that instead of several quantum wells, a period of the device is made from just one quantum well (usually between 30–100 Å wide) separated by a thick barrier (often greater than 200–300 Å) from the next well. The devices work by absorbing photons through electron transitions from the doped quantum wells to the above barrier continuum. From a theoretical viewpoint this is more complicated than QCLs since the transitions occur from two-dimensional confined states in the quantum wells to three-dimensional extended states in the continuum, which would make the description a mixture of two- and three-dimensional states giving complications for the calculation of scattering rates. This is overcome theoretically by 'discretising the continuum' and summing all scattering rate contributions to the transport over more and more closely spaced continuum levels until convergence is acheived [44], see Fig. 7(a).

With this approach the system can again be represented by sets of coupled rate equations which can be solved self-consistently to yield the number of electrons in each state and their distribution up the continuum levels. From this fundamental description all the physical observables of the device can be deduced which includes the responsivity versus wavelength and bias [45]. In particular Fig. 7(b) shows a comparison of calculations of the dark (or noise) current in a $GaAs/Ga_{1-x}Al_xAs$ QWIP designed for absorption at 8.5 μm in comparison with the experimental measurements [46]. It can be seen that the calculations give good agreement on the qualitative form of the relationship between the dark current and the bias as well as good agreement on the absolute magnitude. Further information on other physical observables are available in a recent paper, see [45].

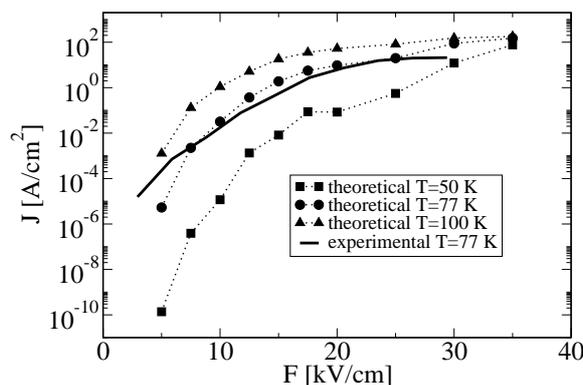# 7. RATE EQUATIONS VERSUS EXPERIMENT IN QUANTUM DOT INFRARED PHOTODETECTORS (QDIPS)

Figure 8. Calculated dependence of the dark current density on the electric field at three different temperatures and the experimental dark current results [47] at $T = 77$K.

Since the initial realization of infrared photodetectors based on quantum dots (QDIPs), there has been a lot of experimental progress, however there has been much less work on theoretical modelling which motivated us to develop a model of electron transport in QDIPs. The QDIP is considered as a periodic superlattice of quantum dots. The energy levels and wave functions belonging to one period are found using the 8-band $\mathbf{k} \cdot \mathbf{p}$ method with the strain distribution taken into account using the continuum mechanical model and found using the finite element method. The populations of energy levels and the current in the device are found from the semiclassical (Boltzmann equation) model, which due to the discreteness of the energy levels reduces to the following system of rate equations:

$$\frac{\mathrm{d}n_i}{\mathrm{d}t} = \sum_{j \neq i} W_{ji} n_j \left(1 - \frac{1}{2} n_i\right) - \sum_{j \neq i} W_{ij} n_i \left(1 - \frac{1}{2} n_j\right) - \sum_j \sigma_{ij}^p(\omega)(n_i - n_j)\Phi, \tag{4}$$

where $0 \leq n_i \leq 2$ is the occupancy of level i including electrons of both spin, W_{ij} is the total transition rate from state i to state j due to interaction with LO and LA phonons calculated as in [15], $\sigma_{ij}^p(\omega)$ is the optical cross

section between states i and j for incident radiation of angular frequency ω and polarization p and Φ is the flux of the incident radiation. The effect of final state blocking is included via the terms $\left(1 - \frac{1}{2}n_i\right)$ that represent the probability that the final state is empty.

From the steady-state solution of the system of rate equations, the population of the energy levels within the dots and in the surrounding discretised continuum were found, in a method similar to our simulations of quantum well infrared photodetectors [16, 45]. Combining these population densities with lifetimes allowed the current density to be calculated. The method was applied to the InAs/GaAs QDIP reported in [47] and the calculated dark current is shown in Fig. 7. The results of the simulation are in agreement with the reported dark current experimental measurements at T=77 K.

8. DENSITY MATRIX MODELLING OF COHERENT TRANSPORT EFFECTS

Despite the success described above of incoherent Boltzmann transport equation approaches to the description of the properties of quantum cascade lasers there has been mounting interest in possible coherent transport effects, particularly in terahertz quantum cascade laser where the small anti-crossing energies may allow resonant tunnelling [48]. Further motivation for this work has been supplied by mounting theoretical arguments for coherent effects, see for example [49, 50].

Our approach to investigate the significance of coherent transport effects is based on the density matrix. Starting from a general quantum kinetic approach which includes the interactions of electrons with longitudinal optical phonons and a classical light field it describes the electron dynamics at the Boltzmann, Markovian and non-Markovian levels of approximation. A full description of our method and the mathematics is available in our recent work [51]; however briefly: we consider electrons in the conduction band of a quantum cascade laser with an external magnetic field applied perpendicular to the layers. This magnetic field localises the electron motion in the plane of the layers and leads to the quantum well subbands splitting into a series of discrete Landau levels. With many Landau levels originating from each quantum well subband there is the potential for the problem to become too demanding computationally to solve. Therefore it is limited by focussing on a device configuration which has relatively few subbands in a period, keeping the temperature low to restrict the number of Landau levels occupied and by introducing a phenomenological damping parameter $\hbar\gamma$ which represents the higher-order correlations in the density matrices.

The quantum kinetics are essentially non-Markovian as the time evolution of the density matrix elements depends on their values at earlier times; i.e. there is a memory effect. The Markovian level of approximation that we also use neglects this memory time effect which stems from the energy-time uncertainty. In each calculation we also recover the semi-classical Boltzmann equations for comparison.

Fig. 9(a) illustrates the active region design chosen for this study. The device is a GaAs/Ga$_{0.7}$Al$_{0.3}$As three quantum well terahertz quantum cascade laser designed to emit at 15.2 meV (equivalent to 3.7 THz or 81 μm) when biased at 16.2 kVcm^{-1}. The design is a simplification of the original injectorless devices of Hu *et al.* [52] and has its peak gain when the ground state (1) is biased into close energy alignment with the upper laser level (3) of the following period.

The electron densities summed over the Landau levels originating from the 3 active region states calculated for the three levels of approximation are shown in Fig. 9(b). It can be seen that for a particular value of the damping parameter ($\hbar\gamma = 1$ meV, say) the predicted populations are quite similar. The generic effect of smoothing out the features of the curves are illustrated by the inclusion of a set of data for the non-Markovian approximation with an increased value of the damping parameter. Of course, the electron densities themselves are not physical observables so it is important to turn attention towards something that may be measured by experiment and the following two figures do just that.

Fig. 10(a) illustrates the results of calculations of the current density through the quantum cascade laser region as a function of magnetic field for the fixed (design) bias field of 16.2 kVcm^{-1}. It can be seen from the figure that the Boltzmann and Markovian approximations yield very similar results. Whilst the non-Markovian data has a higher and broader peak, without the shoulder at 7 T, it is unlikely that given a measurement on a device that a comparison between theory and experiment could allow identification of the mode of quantum
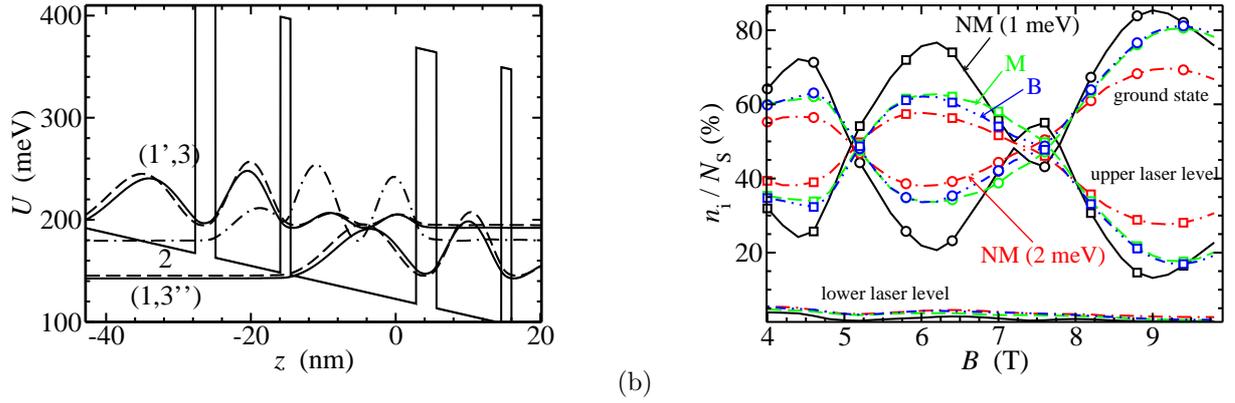
Figure 9. (a)A schematic diagram of the probability distributions of the active region of the GaAs/Ga$_{1-x}$Al$_x$As quantum cascade laser biased at 16.2 kVcm^{-1} and at zero magnetic field. The ground state (1) is depicted by a solid line, the lower laser level (2) by a dashed-dotted line and the upper laser level (3) by a dashed line. State 1' belongs to the preceding period and state 3" to the following period (b) The electron densities n_i summed over all Landau Levels as a percentage of the total sheet density N_s per period for Landau Levels associated with the ground state, lower and upper laser levels. The letters 'B', 'M' and 'NM' denote the Boltzmann, Markovian and Non-Markovian levels of approximation respectively for a damping parameter $\hbar\gamma$ equal to 1 meV. The figure also shows the corresponding data for the Non-Markovian approximation for $\hbar\gamma = 2$ meV.
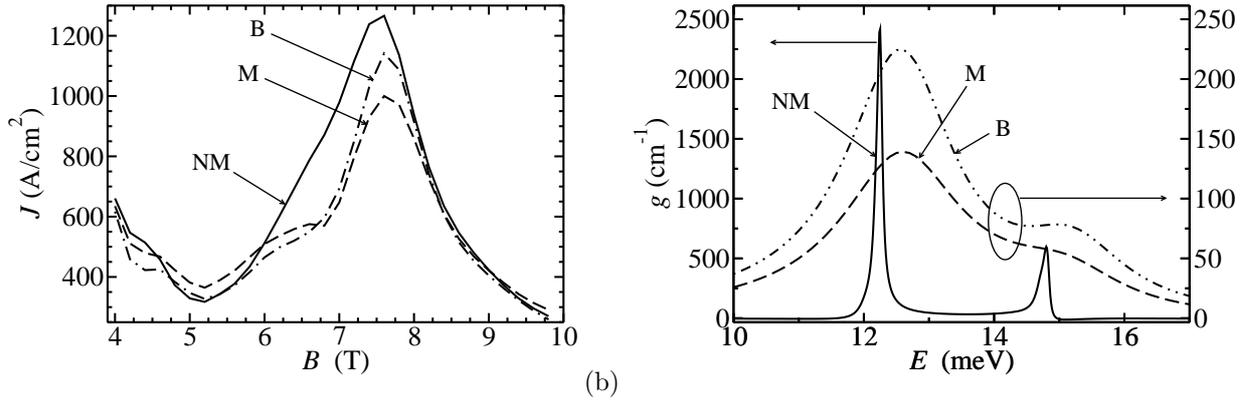

Figure 10. (a) The electric current as a function of magnetic field at the design bias of 16.2 kVcm^{-1}. Again 'B', 'M' and 'NM' denote Boltzmann, Markovian (M) and Non-Markovian levels of approximation respectively. The dampling parameter $\hbar\gamma$ is equal to 1 meV., (b) The optical gain versus energy around the lasing transition at a magnetic field of 4 T. Note the data for the Boltzmann (B) and Markovian (M) approximations are represented on the right-hand axis and the Non-Markovian (NM) on the left-hand axis. The dampling parameter $\hbar\gamma$ is equal to 1 meV.

transport. However, the same is not true for the predictions of the optical gain versus energy (or wavelength) around the lasing transition which are shown in Fig. 10(b).

Fig. 10(b) does again show that the predictions of the Boltzmann and Markovian approximations to the density matrix are quite similar; however in these calculations the predicted optical gain versus energy (or wavelength) for the non-Markovian approach is quite distinct. Rather than just a broad gain profile with a shoulder; the non-Markovian data shows two clearly resolved sharp peaks. Measurements of this type have been

performed for quantum cascade lasers, see for example [53]; however they are difficult to perform and require a broad band terahertz source to provide the excitation across a range of energies around the lasing transition, hence experiments of this type are quite infrequent. We propose that a joint effort between theory and experiment be made to shed light on the nature of the electron transport in these devices.

9. CONCLUSION

The full Monte Carlo simulations of the carrier distributions across the quantum well subbands of biased semiconductor heterostructures have substantiated our rate equation calculations discussed here and elsewhere, and indicate that in unipolar optoelectronic devices at room temperature the electrons or holes within a band or subband can be represented to a good approximation by a Fermi-Dirac distribution. However, the latter are generally specific to a particular band or subband and certainly have their own quasi-Fermi energy. In addition, the temperature characterising each of these distributions in the steady-state is above that of the lattice and can be calculated by assuming equilibrium in the phonon generation rate (energy balance). It has been found that in the class of devices which includes quantum cascade lasers and quantum well infrared photodetectors, the physical observables can be predicted to good accuracy by assuming the same electron temperature across the series of subbands.

Perhaps more important than the successful comparison with the Monte Carlo simulations, is the validation of the rate equations approach with experimentally measured physical observables. It must be noted that the only inputs to these calculations are materials constants such as the well and barrier widths, the barrier heights, the effective masses, dielectric constants, LO phonon energy, etc. and the calculations are able to predict observables such as saturation, dark and threshold currents, laser gain, etc. without adjusting any parameters to achieve a best fit. The only instance of a parameter entering the process is in the case of interface roughness scattering where the correlation length may vary from heterostructure to heterostructure so a single value was taken from an experimental paper. Thus the conclusion must be that, given that the methods are successful in explaining experimental data then the *a priori* assumption that the transport is dominated by *incoherent* carrier scattering is true.

However, in order to satisfy the authors' curiosity and for completeness we have also developed a model of the electron transport in quantum cascade laser based on the density matrix approach. Again for thoroughness we have performed calculations at the Boltzmann, Markovian and non-Markovian levels of approximation. The first two of these produce quite similar, certainly experimentally indistinct, results and aid in model validation. Whilst the latter predicts current densities similar to the Boltzmann and Markovian cases it predicts a quite different optical gain spectrum. We propose that further measurements of this effect be coupled with a coordinated theoretical effort to see if transport in quantum cascade lasers in certain instances has aspects of coherence and is better described by non-Markovian dynamics.

REFERENCES

1. R. Köhler, A. Tredicucci, F. Beltram, H. E. Beere, E. H. Linfield, A. G. Davies, D. A. Ritchie, R. C. Iotti, and F. Rossi, "Terahertz semiconductor heterostructure laser," *Nature* **417**, p. 156, 2002.
2. C. Walther, M. Fischer, G. Scalari, R. Terazzi, N. Hoyler, and J. Faist, "Quantum cascade lasers operating from 1.2 to 1.6 THz," *Applied Physics Letters* **91**, p. 131122, 2007.
3. G. Scalari, C. Walther, H. Beere, D. Ritchie, and J. faist, "Laser emission at 830 and 960 ghz from quantum cascade structures," in *The Proceedings of the Ninth International Conference on Intersubband Transitions in Quantum Wells*, D. Indjin, Z. Ikonić, P. Harrison, and R. W. Kelsall, eds., p. T15, 2007.
4. H. Page, C. Backer, A. Roberston, G. Glastre, V. Ortiz, and C. Sirtori, "300 k operation of a gaas-based quantum-cascade laser at λ approximate to 9 μm," *Appl. Phys. Lett.* **78**, p. 3529, 2001.
5. C. Pflügl, W. Schrenk, S. Andres, G. Strasser, C. Becker, C. Sirtori, Y. Bonetti, and A. Muller *Appl. Phys. Lett.* **83**, p. 4698, 2003.
6. S. Andres, W. Schrenk, E. Gornik, and G. Strasser *Appl. Phys. Lett.* **80**, p. 1864, 2002.
7. H. Page, S. Dhillon, M. Calligaro, C. Becker, V. Ortiz, and C. Sirtori *IEEE J. Quantum Elec.* **40**, p. 665, 2004.

8. R. C. Iotti and F. Rossi, "Nature of charge transport in quantum-cascade lasers," *Phys. Rev. Lett.* **87**, p. 146603, 2001.

9. P. Harrison and R. W. Kelsall, "The relative importance of electron-electron and electron-phonon scattering in terahertz quantum cascade lasers," *Solid State Electronics* **42**, pp. 1449–1451, 1998.

10. P. Harrison, "The nature of the electron distribution functions in quantum cascade lasers," *Appl. Phys. Lett.* **75**, pp. 2800–2802, 1999.

11. Z. Ikonic, P. Harrison, and R. W. Kelsall, "Intersubband hole-phonon and alloy disorder scattering in sige quantum wells," *Phys. Rev. B* **64**, p. article 245311, 2001.

12. H. Callebaut and Q. Hu, "Importance of coherence for electron transport in terahertz quantum cascade lasers," *J. Appl. Phys.* **98**, p. 104505, 2005.

13. T. Kuhn and F. Rossi, "Monte carlo simulation of ultrafast processes in photoexcited semiconductors: Coherent and incoherent dynamics," *Phys. Rev. B* **46**, pp. 7496–7514, 1992.

14. C. Jacoboni and L. Reggiani *Rev. Modern Phys.* **55**, p. 645, 1983.

15. N. Vukmirović, Z. Ikonić, V. D. Jovanović, D. Indjin, and P. Harrison, "Optically pumped intersublevel midinfrared lasers based on inas-gaas quantum dots," *IEEE J. Quan. Elec.* **41**, pp. 1361–1368, 2005.

16. I. Savić, V. Milanović, N. Vukmirović, V. D. Jovanović, Z. Ikonić, D. Indjin, and P. Harrison, "Magnetic-field tunable terahertz quantum well infrared photodetector," *J. Appl. Phys.* **98**, p. 084509, 2005.

17. R. W. Kelsall, Z. Ikonić, P. Harrison, S. A. Lynch, R. Bates, D. J. Paul, D. J. Norris, S. L. Liew, A. G. Cullis, D. J. Robbins, P. Murzyn, C. R. Pidgeon, D. D. Arnone, and R. A. Soref, "Terahertz emission from silicon-germanium quantum cascades," in *Towards the first Silicon laser*, L. P. et al, ed., Kluwer, 2003.

18. R. W. Kelsall and R. A. Soref, "Silicon germanium quantum cascade lasers," in *Terahertz Sensing Science and Technology*, D. L. Woolard, W. R. Loerop, and M. S. Shur, eds., **1**, World Scientific, 2003.

19. Z. Ikonic, R. W. Kelsall, and P. Harrison, "The virtual crystal approximation and alloy broadening of intersubband transitions in *p*-type sige quantum wells," *Phys. Rev. B* **64**, p. article number 125308, 2001.

20. Z. Ikonić, R. W. Kelsall, and P. Harrison, "Monte carlo simulations of hole dynamics in sige/si terahertz quantum-cascade structures," *Phys. Rev. B* **69**, p. article 235308, 2004.

21. Z. Ikonić, P. Harrison, and R. W. Kelsall, "Self-consistent energy balance simulations of hole dynamics in sige/si thz quantum cascade structures," *J. Appl. Phys.* **96**, pp. 6803–6811, 2004.

22. Z. Ikonić, P. Harrison, and R. W. Kelsall, "Electric field domains in *p*-si/sige quantum cascade structures," *IEEE Trans. Electron Devices* **53**, pp. 189–195, 2006.

23. R. C. Iotti and F. Rossi, "Carrier thermalisation versus phonon-assisted relaxation in quantum cascade lasers: A monte carlo approach," *Appl. Phys. Lett.* **78**, p. 2902, 2001.

24. K. Donovan, P. Harrison, and R. W. Kelsall, "Self-consistent solution to the intersubband rate equations in quantum cascade lasers: Analysis of a gaas/al$_x$ga$_{1-x}$as device," *J. Appl. Phys.* **89**, pp. 3084–3090, 2001.

25. D. Indjin, P. Harrison, R. W. Kelsall, and Z. Ikonic, "Self-consistent scattering theory of transport and output characteristics of quantum cascade lasers," *J. Appl. Phys.* **91**, pp. 9019–9026, 2002.

26. D. Indjin, P. Harrison, R. W. Kelsall, and Z. Ikonić, "Mechanisms of temperature performance degradation in terahertz quantum-cascade lasers," *Appl. Phys. Lett.* **82**, pp. 1347–1349, 2003.

27. P. Harrison, D. Indjin, and R. W. Kelsall, "The electron temperature and mechanisms of hot carrier generation in quantum cascade lasers," *J. Appl. Phys.* **92**, pp. 6921–6923, 2002.

28. R. Köhler, A. Tredicucci, F. Beltram, H. E. Beere, E. H. Linfield, A. G. Davies, and D. A. Ritchie, "High intensity interminiband terahertz emission from chirped superlattice," *Appl. Phys. Lett.* **80**, p. 1867, 2002.

29. H. Sakaki, T. Noda, K. Hirakawa, M. Tanaka, and M. Matsusue *Appl. Phys. Lett.* **51**, p. 1934, 1987.

30. T. Unuma, M. Yoshita, T. Noda, H. Sakaki, and H. Akiyama *J. Appl. Phys.* **93**, p. 1586, 2003.

31. M. S. Vitiello, V. Spagnolo, G. Scamarcio, B. Williams, S. Kumar, Q. Hu, and J. L. Reno in *6th International Conference on Midinfrared Optoelectronics, Materials and Devices*, (St. Petersburg, Russia), 2004.

32. S. Kumar, B. S. Williams, S. Kohen, Q. Hu, and J. L. Reno *Appl. Phys. Lett.* **84**, p. 2494, 2004.

33. R. Köhler, R. C. Iotti, A. Tredicucci, and F. Rossi *Appl. Phys. Lett.* **79**, p. 3920, 2001.

34. B. S. Williams, S. Kumar, H. Callebaut, Q. Hu, and J. L. Reno *Appl. Phys. Lett.* **83**, p. 207, 2003.

35. H. Callebaut, S. Kumar, B. S. Williams, and Q. Hu *Appl. Phys. Lett.* **84**, p. 645, 2004.

36. O. Bonno, J.-L. Thobel, and F. Dessenne *J. Appl. Phys.* **97**, p. 043702, 2005.

37. V. D. Jovanović, D. indjin, N. Vukmirović, Z. Ikonić, P. Harrison, E. H. Linfield, H. Page, X. Marcadet, C. Sirtori, C. Worrall, H. E. Beere, and D. A. Ritchie, "Mechanisms of dynamic range limitations in gaas/algaas quantum-cascade lasers: Influence of injector doping," *Appl. Phys. Lett.* **86**, p. 211117, 2005.

38. S. Höfling, V. Jovanović, D. Indjin, J. Reithmaier, A. Forchel, Z. Ikonić, N. Vukmirović, P. Harrison, A. Mirčetić, and V. Milanović, "Dependence of saturation effects on electron confinement and injector doping in GaAs/ AlGaAs quantum-cascade lasers," *Applied Physics Letters* **88**, p. 251109, 2006.

39. K. Ohtani, Y. Moriyasu, H. Ohnishi, and H. Ohno, "Above room-temperature operation of InAs/ AlGaSb superlattice quantum cascade lasers emitting at 12 μm," *Applied Physics Letters* **90**, p. 261112, 2007.

40. E. Mujagic, M. Austere, S. Schartner, M. Nobile, W. Schrenk, G. Strasser, I. Bayrakli, M. P. Semtsiv, and W. T. Masselink, "Doping density dependent performance of short-wavelength inp quantum-cascade lasers," in *The Proceedings of the Ninth International Conference on Intersubband Transitions in Quantum Wells*, D. Indjin, Z. Ikonić, P. Harrison, and R. W. Kelsall, eds., p. P10, 2007.

41. V. D. Jovanović, S. Höfling, D. Indjin, N. Vukmirović, Z. Ikonić, P. Harrison, J. P. Reithmaier, and A. Forchel, "Influence of doping density on electron dynamics in gaas/algaas quantum cascade lasers," *J. Appl. Phys.* **99**, p. 103106, 2006.

42. V. Spagnolo, G. Scamarcio, H. Page, and C. Sirtori, "Simultaneous measurement of the electronic and lattice temperatures in GaAs/AlGaAs quantum-cascade lasers: Influence on the optical performance," *Applied Physics Letters* **84**, p. 3690, 2004.

43. G. Sarusi, A. Carbone, S. D. Gunapala, and H. C. Liu, eds., *Proceedings of the Workshop on Quantum Well Infrared Photodetectors*, (Amsterdam), Elsevier, 2002.

44. N. E. I. Etteh and P. Harrison, "Quantum mechanical scattering investigation of the thermionic and field induced emission components of the dark current in quantum well infrared photodetectors (qwips)," *J. App. Phys.* **92**, pp. 248–252, 2002.

45. V. D. Jovanović, P. Harrison, Z. Ikonić, and D. Indjin, "Physical model of quantum-well infrared photodetectors," *J. Appl. Phys.* **96**, pp. 269–272, 2004.

46. L. Thibaudeau, P. Bois, and J. Y. Duboz *J. Appl. Phys.* **79**, p. 446, 1996.

47. Z. Chen, O. Baklenov, E. T. Kim, I. Mukhametzhanov, J. Tie, A. Madhukar, Z. Ye, and J. C. Campbell, "Normal incidence InAs/Al$_x$Ga$_{1-x}$As quantum dot infrared photodetectors with undoped active region," *J. Appl. Phys.* **89**, pp. 4558–4563, 2001.

48. H. Callebaut and Q. Hu, "Importance of coherence for electron transport in terahertz quantum cascade lasers," *Journal of Applied Physics* **98**, p. 104505, 2005.

49. I. Waldmueller, W. Chow, and A. Knorr, "Influence of radiative coupling on coherent Rabi intersubband oscillations in multiple quantum wells," *Physical Review B* **73**(3), p. 35433, 2006.

50. S. Butscher, J. Förstner, I. Waldmüller, and A. Knorr, "Ultrafast electron-phonon interaction of intersubband transitions: Quantum kinetics from adiabatic following to Rabi-oscillations," *Physical Review B* **72**(4), p. 45314, 2005.

51. I. Savić, N. Vukmirović, Z. Ikonić, D. Indjin, R. Kelsall, P. Harrison, and V. Milanović, "Density matrix theory of transport and gain in quantum cascade lasers in a magnetic field," *Phys Rev B* **76**, p. 165310, 2007.

52. B. Williams, S. Kumar, H. Callebaut, Q. Hu, and J. Reno, "3.4 THz quantum cascade laser operating above liquid nitrogen temperature," *Electronics Letters* **39**(12), pp. 915–916, 2003.

53. R. Terazzi, T. Gresch, M. Giovannini, N. Hoyler, N. Sekine, and J. Faist, "Bloch gain in quantum cascade lasers," *NATURE PHYSICS* **3**(5), p. 329, 2007.